TITLE PAGE

Title: Forearc seismogenesis and plate coupling in subduction zone influenced by slab mantle fluids

Author List: Darcy Cordell[1,2], Samer Naif[1], Rob Evans[3], Kerry Key[4], Steven Constable[5], Donna Shillington[6], Anne Bécel[4]

Affiliations:

[1] School of Earth and Atmospheric Sciences, Georgia Institute of Technology, Atlanta, GA 30318, USA

[2] Department of Physics, University of Alberta, Edmonton, AB, Canada T6G 2R3

[3] Department of Geology and Geophysics, Woods Hole Oceanographic Institution, Woods Hole MA 02543, USA.

[4] Lamont-Doherty Earth Observatory, Columbia University, Palisades, NY 10964, USA

[5] Scripps Institution of Oceanography, La Jolla, CA 92037, USA

[6] School of Earth and Sustainability, Northern Arizona University, Flagstaff, AZ 86011, USA

Corresponding Author: Darcy Cordell, dcordell6@gatech.edu

ABSTRACT

The role of fluids in earthquake rupture is key to understanding seismic hazards, particularly at subduction zones. The Shumagin Gap, Alaska, is notable due to a paucity of large earthquake nucleation and weak coupling between the overriding and subducting plates. Fluids have been hypothesized to explain these observations, however the source of fluids remains unclear. Here, we present an image of the subsurface electrical resistivity derived from marine magnetotelluric data collected in the Shumagin segment. The model reveals a ~50-km-wide conductive (i.e. fluid-rich) zone near the plate interface with fluids sourced from dehydration of slab mantle (15–25 km beneath crust-mantle boundary). We find that the July 2020 megathrust earthquake—which nucleated near the Semidi segment and propagated westward into the Shumagin segment—only ruptured the conductive portion of the plate interface. This suggests slab mantle fluids can influence the seismogenic zone by, e.g., creating patches prone to dynamic rupture. In contrast, updip of the slip patch is simultaneously resistive and weakly-coupled, suggesting fluids alone are not responsible for weak coupling, and plate roughness plays a role. More broadly, these results suggest slab mantle fluids can be an underappreciated fluid source in forearc subduction zone water budgets.

MAIN TEXT

Fluids in subduction zones influence many important geological processes as the hydrated incoming plate is subducted beneath the overriding crust and mantle wedge, and cycles water deep into Earth's mantle[1]. As the slab enters the subduction zone, shallow pore-bound water is released by compaction[2]. At greater pressures and temperatures, chemically-bound water in the subducted sediments, crust and mantle is released via dehydration reactions as hydrous minerals undergo prograde metamorphism[1]. Where and when water is released, as well as the quantity and transport of such water, has important implications for Earth's global water budget, the properties of the overlying mantle wedge, flux melting that feeds arc volcanism, and earthquake slip behaviour in the seismogenic zone[1–3].

Of particular interest are the properties of the subducting plate that trigger either fault creep or significant seismic rupture. Previous studies indicate a correlation between the presence of fluids and low plate coupling since fluids lubricate faults and promote creep[4–7]. However, while fluids at the plate interface can lower the effective normal stress they can also create conditionally stable regions which have strain-dependent slip behavior[8]. During punctuated, high-strain events associated with nearby megathrust earthquake rupture, a critical threshold is reached, and large fault slip may propagate into conditionally-stable, fluid-rich regions either up-dip[9] or along-strike[10]. The roughness of the plate interface has also been suggested to have a control on megathrust slip, with rough plate interfaces facilitating fault creep, while smooth plate interfaces are prone to stick-slip behavior[11]. An interplay of these factors likely contributes to both inter-seismic and co-seismic slip behavior.

The Shumagin segment (*Fig. 1*) is unique along the Alaska-Aleutian forearc for its abundant low-intensity seismicity but lack of large (>8 Mw) megathrust ruptures nucleating in the segment. This has led to various authors referring to the Shumagin segment as a "seismic gap"[12]. Geodetic data suggest that the Shumagin segment is weakly coupled relative to the adjacent Semidi segment, and that a large fraction of strain is accommodated by fault creep[13]. Several hypotheses have been put forward to explain the paucity of large megathrust earthquakes and the weakly-coupled plate interface, including changes in incoming plate fabric, sediment thickness, slab dip and/or degree of hydration on the incoming plate[14–20]. Related to these hypotheses is that excess fluids enter the subduction zone in the Shumagin segment and promote fault creep and low coupling coefficients[15,16,20]. However, pore pressure estimates from seismic observations of the shallow megathrust (<10 km depth) indicate a lack of over-pressured fluids and suggest plate roughness promotes fault creep in the Shumagin segment[21]. In this case, a rough, more permeable slab crust could more effectively drain the plate interface such that a fluid-poor megathrust fault with abundant, small-scale asperities promotes creep and low coupling coefficients[11]. As such, it is unclear whether the paucity of large megathrust earthquakes is due to fluid-rich or fluid-poor conditions, and whether these same conditions promote weak plate coupling.

While some amount of the strain in the Shumagin segment appears to be accommodated by fault creep rather than rupture in great earthquakes, a recent seismic doublet occurred in 2020. In July 2020, a Mw 7.8 megathrust earthquake nucleated within (or near the boundary of) the Semidi segment and then ruptured trench-parallel deeper into the Shumagin segment (*Fig. 1*)[14,22–25]. This event was followed by a Mw 7.6 strike-slip earthquake in October 2020 oriented perpendicular to the trench, within the downgoing slab, and updip of the earlier rupture[14]. While the July 2020 earthquake did partially fill the Shumagin "gap"[23], it is important to emphasize: (a) it did not nucleate deeply within the gap and instead nucleated within (or near) the more strongly-coupled Semidi segment and (b) the Shumagin segment has still not experienced a historical large event which ruptures the entire plate interface akin to those in adjacent segments throughout the Alaska-Aleutian subduction zone.

A landward-dipping normal fault in the overriding plate separates the Cretaceous-age Chugach Terrane from the younger, Paleocene Prince William Terrane (PWT)[18,19]. Activity on the fault led to the formation of the Sanak Basin, a Miocene-age half-graben structure with ~6 km of sediments[18]. The fault cuts through the entire overriding plate and intersects the plate interface near the continental Moho where an anomalous band of reflectors was identified with multichannel seismic (MCS) reflection data[17]. This band of reflectors is hypothesized to be due to anomalous fluids and/or underplating near the continental Moho[17,19].

To better constrain the distribution of fluids in the Shumagin segment, we collected marine magnetotelluric (MT) data[26] along a 250-km trench-perpendicular profile in 2019 (*Fig. 1*). The MT method is ideally suited to imaging subduction zone structures because it is sensitive to the presence of electrically conductive aqueous fluids relative to resistive dry igneous rock[5–7,27,28]. MT data are also useful in their ability to distinguish between hydrated mantle and free fluids since serpentine minerals such as antigorite are resistive[29]. As shown in Extended Data Figs. 1-3, MT data collected outboard of the shelf break were not amenable to 2-D modelling. Thus, we inverted 23 MT sites for isotropic electrical resistivity structure on the forearc shelf using 2-D inversion (see Methods). Various model parameters were tested including resolution and sensitivity tests (see Extended Data Figs. 4-10).

Forearc Electrical Structure

Our preferred resistivity model[26] (*Fig. 2*) contains several features that correlate with independent geophysical constraints in the overriding plate. The East Sanak Basin on the southern end of the profile is relatively conductive with the bottom of conductor C1 following the basin floor as interpreted from seismic reflection, and thinning to the north[18]. The Chugach Terrane in the overriding plate is very resistive (>1,000 Ωm), while the PWT is moderately resistive (~100–1,000 Ωm). The region around the plate interface is broadly conductive 90–150 km from the trench (i.e., 25–35 km depth). At 130 km from the trench, there is a prominent conductor (C2) directly above the plate interface. Directly beneath C2 is another prominent conductor (C3) located in the slab mantle, centered approximately 20 km beneath the oceanic Moho.

The location of C2 and the broadly conductive zone 90–150 km from the trench indicates that this portion of the Shumagin segment is fluid-rich, whereas the resistive parts of the plate interface updip and down-dip are relatively fluid-starved. C2 is interpreted as a particularly fluid-rich zone and aligns with the band of thick reflectors identified in the co-located MCS data[17]. C2 also aligns with the intersection of the crustal-scale normal fault separating the Chugach Terrane and PWT in the overriding plate. The normal fault may allow fluids from C2 to escape along the more steeply-dipping permeable pathway rather than migrating updip along the megathrust fault[18]. Indeed, the MT model does indicate that the pathway along the normal fault is moderately more conductive than the adjacent Chugach Terrane and PWT, although poor resolution inhibits us from making a more conclusive claim about fluids along the normal fault.

Fluid Distribution and Slip Behavior

The July 2020 megathrust earthquake nucleated to the east and ruptured trench-parallel through the conductive region and did not experience coseismic rupture updip or downdip into the resistive parts of our MT model (*Fig. 2*). The slip distribution coincides with the conductive region 90–150 km from the trench, and the peak co-seismic slip aligns with the most conductive (i.e., fluid-rich) region near C2 (*Fig. 2*). This observation runs contrary to expectation since fluid-rich segments have generally been interpreted to be regions of weaker coupling and fault creep which are less prone to rupture[4,5,7]. However, the July 2020 earthquake nucleated to the east, relatively close to the epicenters of previous >8 Mw ruptures and the strongly-coupled Semidi segment[22,23]. One possibility to explain these observations is that the fluid-rich region promotes areas of conditional stability where ruptures propagate along-strike through the fluid-rich region due to dynamic weakening rather than propagating up-dip[8]. This does not necessarily contradict slip models which assume stress build-up on a more strongly-coupled frictional asperity since small asperities (e.g. beneath the Shumagin Islands) could be embedded in a broader region of conditional stability[24]. Geodetic studies indicate that asperities decrease in size moving westwards from the Semidi segment to the Shumagin segment, with the relative area of conditionally stable patches increasing, in agreement with our interpretation[15]. The fluids in the Shumagin segment may act to lubricate faults and promote fault creep during interseismic periods, which would inhibit rupture nucleation, but can dynamically weaken during co-seismic slip[8]. Similar conditionally-stable patches driven by increased pore-fluid pressures have been observed elsewhere such as at the Hikurangi and Nankai margins[10,30].

In contrast, the shallow plate interface (<25 km depth) is resistive, indicating a lack of fluids, and the July 2020 megathrust earthquake did not rupture updip into the resistor. This suggests that the lack of fluids in the upper portions of the megathrust fault may inhibit rupture propagation. A fluid-starved shallower plate interface is consistent with results from an MCS reflection study which imaged a rough shallow plate interface with inferred low pore pressures within 25 km of the trench[21]. A rough plate interface extending deeper, to 120 km from the trench, is also indicated by high-velocity intrusions[19]. Thus, the plate interface may be relatively rough throughout the Shumagin segment which contributes to a decrease in coupling overall[11]. This suggests that fluids and plate roughness can independently contribute to lowering plate coupling, although the presence of fluids may make a rough plate conditionally stable and thus influence rupture propagation. In the case of the Shumagin segment, the lack of fluid-driven conditional stability updip may inhibit rupture propagation towards the trench, with ruptures propagating along-strike instead. This is in contrast to e.g. northeast Japan where the 2011 Tohoku-oki earthquake ruptured updip into a zone of fluid-driven conditional stability[9].

Finally, there is a notable cluster of earthquakes that occurs on the down-dip edge of C2 (~135–150 km from the trench), where the MT model has a high conductivity gradient with structure quickly becoming resistive. The high conductivity gradient is also where the continental Moho intersects the plate interface, indicating that the megathrust lithology transitions to dry mantle downdip based on its high resistivity. This suggests that a change in structural characteristics from fluid-rich and weak (i.e. conductive) to fluid-poor and strong (i.e. resistive) causes a sudden onset of deformation and stress leading to abundant small-scale seismicity. This change in structural characteristics may promote greater coupling on the downdip side of C2, which in turn could produce extensional forces in the upper plate leading to the formation of the crustal normal fault[18].

The Source of Fluids

Fluids near the plate interface in the seismogenic zone are often assumed to be derived from subducted sediments and slab crust due to compaction and/or prograde metamorphic reactions of their respective hydrous mineral assemblages, whereas slab mantle dehydration is thought to occur beneath the arc and backarc[1]. However, a prominent conductor (C3) at 60 km depth in our MT model is centered 20 km beneath the slab Moho and ~125 km from the trench, beneath the shallower conductor near the plate interface (C2) (*Fig. 2*). The location of C3 suggests that fluids are present much deeper in the slab mantle and buoyantly rise to the shallower forearc plate interface in the Shumagin segment (*Fig. 2*). Fluids near the plate interface (e.g. C2) are unlikely to be due wholly to C3, with some *in situ* dehydration processes occurring in the slab crust, but it appears that rising fluids from C3 provide an anomalous source of fluids for the Shumagin segment. This observation implies that the forearc slab mantle is a previously unrecognized source of water in the forearc which may impact subduction zone water budgets and, in turn influence seismogenic zone behavior.

Seismic imaging at the outer rise of the Shumagin segment suggests there is substantial serpentinization of the incoming slab mantle several kilometers sub-Moho, below which the data lose sensitivity[15,19]. Hydration of the Shumagin slab mantle has been hypothesised to be caused by fluid ingress along reactivated, pre-existing, trench-aligned plate fabric, and subducted transform faults related to the Resurrection-Kula spreading center[14,16]. Because recent seismic images on the incoming plate at other subduction zones suggest deeper mantle hydration (e.g. 10–30 km sub-Moho) is possible at the outer rise[31–33], this may also be the case at the Shumagin segment. However, previous authors have not considered the fate of these deeply hydrated slabs.

Using a thermal petrologic model[3], we constructed the pressure-temperature (P-T) pathway of the subduction zone at 20±5 km sub-Moho for the Shumagin segment, along with hydrous mineral stability fields within hydrated ultramafic rocks from several laboratory experiments[34–39]. As shown in *Fig. 3a*, there is substantial variability in the stability fields depending on the choice of mineral composition and laboratory experiment, yet *Fig. 3b* demonstrates that the range of P-T paths at C3 overlap significantly with the hydrous mineral stability fields from experiments. Given the uncertainties associated with the thermal structure and slab geometry[40], the precise position of C3, the variabilities in bulk-rock composition and fluid-content effects on dehydration[37,41], and the simplifications regarding the reaction kinetics[42], it is plausible that C3 is due to fluids derived from dehydration in the forearc slab mantle. This is only possible if fluids reached depths of >15 km, otherwise forearc P-T conditions in the Shumagin segment are likely too cold and serpentinite would remain stable until arc or back-arc depths. In addition, C3 is localized, which suggests that resolvable quantities of fluids are not present updip or downdip. This may be because C3 represents a discrete pulse of dehydration related to over-stepping antigorite dehydration reactions[42], and/or anomalous mineralogy related to inherited structures with modified bulk compositions (e.g. deep hydration associated with subducted Kula spreading center[14,43,44]).

Regardless of the mechanism for how fluids arrived at C3, our model suggests that forearc slab mantle fluids migrate upwards towards the plate interface and influence seismogenic zone behavior. The fluids would not necessarily hydrate (i.e. serpentinize) the slab mantle above C3 if they are channelized along existing fractures, faults and veins[45]. Note that the low bulk resistivity of C3 does not necessarily imply a large volume of homogeneously-distributed fluids, since a well-connected network of saline fluids which occupies a small total volume can still decrease the bulk resistivity substantially[46]. Constraints on the composition of dehydration fluids as they migrate and react with the surrounding slab mantle are needed to reliably quantify the porosity of C3.

As summarized in the conceptual model of *Fig. 4*, free fluids in the slab mantle (C3) percolate upwards along sub-vertical paths toward the plate interface (C2)[1]. These results raise several important questions about the subduction zone fluid cycle and the source of forearc fluids. Our observations suggest that deeply hydrated incoming plates can provide an underappreciated source of fluids to the forearc seismogenic zone, although the physical processes which allow for such deep hydration at the outer rise are challenging to explain[47].

While the MT model does not definitively image fluids along the crustal-scale normal fault separating the Chugach Terrane from the PWT, the region is moderately conductive relative to the adjacent terranes, which does not preclude the possibility that the fault may act as a conduit for fluids from C2 (*Fig. 4*). We hypothesize that seeps at the fault outcrop have a slab mantle isotopic signature. Most geochemical studies interpret mantle signatures in forearc fluids as the result of deeper (i.e. downdip) dehydration from the slab crust moving updip along the plate interface and picking up mantle geochemical signals in transit as they are flushed through the mantle wedge—often over long distances[48,49]. Our results suggest an alternative explanation that slab mantle fluids are present directly beneath the forearc and have no interaction with the mantle wedge.

Delivery of anomalous slab mantle fluids to the seismogenic zone appears to modulate and segment slip behavior in the Shumagin segment and help explain the cause of the anomalous reflectivity in seismic images. The addition of these fluids to the plate interface may result in conditionally stable patches. During proximal, high strain events—such as the July 2020 megathrust earthquake—the fluids provide a path for the megathrust rupture to propagate parallel to the trench more deeply into the creeping Shumagin segment where small-scale asperities may also be present. Co-seismic slip is confined to the fluid-rich portions of the seismogenic zone rather than rupturing updip. Fluids thus help explain several geodetic observations including the lack of updip rupture, and the increasing size of conditionally stable patches to the west[24]. In contrast to the correlation between fluid distribution and plate coupling observed at other subduction zones[5,7], the fluid-starved plate interface updip (<30 km depth) is weakly-coupled indicating that fluids are not required for weak coupling. This highlights the complex interplay of factors that control the seismogenic zone behaviour, and suggests that fluid-rich regions in weakly coupled subduction zones may still be seismically hazardous.

ACKNOWLEDGEMENTS

We thank the captain and crew of the R/V Sikuliaq expedition SKQ201914S, the Scripps Marine EM Lab (Chris Armerding, Jacques Lemire, Jacob Perez, John Souders) and the EMAGE science party (Tanner Acquisto, Julen Alvarez-Aramberri, Janine Andrys, Chris Armerding, Eric Attias, Goran Boren, Brandon Chase, Christine Chesley, Peter K. Miller, Jacob Perez, Li Wei, and Jasmine Zhu). We greatly appreciate the helpful suggestions from the editors as well as three anonymous reviewers. This work was supported by the National Science Foundation grants OCE-1654652 to KK, SC, SN, and DS, and OCE-1654619 to RE.

AUTHOR CONTRIBUTIONS

K.K., R.L.E, S.C., and S.N. designed the experiment. K.K., S.C., and S.N. collected the data. S.N. processed the MT responses. D.C. modelled the data, produced the figures, and wrote the initial manuscript. All authors discussed the results and contributed to writing the manuscript.

COMPETING INTERESTS

The authors have no competing interests to declare.

FIGURE LEGENDS

Figure 1: *Map of the Shumagin segment study area. White circles are magnetotelluric (MT) site locations on the forearc shelf used in this study, while red circles are MT sites excluded. Black dots are 2010-2021 epicenters*[50]*. Black, magenta and green lines are aftershock zones from >8 Mw ruptures in adjacent segments*[12,51]*. Red and yellow lines are slip patches from July 2020 and October 2020, respectively*[23,51]*. Thin white lines show faults bounding the East Sanak Basin*[52]*. Dashed grey contours are slab depths from Slab2.0*[53]*. Beach balls are global centroid moment tensor solutions for the July 2020, and July 2021 earthquakes*[54]*. The yellow star shows the USGS epicenter for the July 2020 earthquake*[51]*.*

Figure 2: (A) *Resistivity model for the Shumagin segment of the Alaska-Aleutian subduction zone. Background color is resistivity with thin black contours in 0.5 log unit intervals. White lines are co-located seismic P-wave velocity contours in km/s and thick black dashed lines are the top and bottom of the slab crust from the refraction tomography model*[19]*. The co-located MCS seismic reflection*[18] *is overlain, from which structural interpretations are derived (thin black dashed lines), such as the normal fault separating the Prince William Terrane (PWT) from the Chugach Terrane and a thick band of reflectors at the plate interface (circled). White circles are seismicity within 30 km of the profile from ref.* [50]*. Red triangles are MT site locations. Labelled conductivity anomalies C1, C2, and C3 are discussed in text. (B) Total slip from the July 2020 megathrust earthquake along the MT profile from three different co-seismic slip models*[22,23,25]*, as well as a histogram of total number of earthquakes along the profile.*

Figure 3: *Hydrous mineral dehydration and slab pressure-temperature (P-T) paths for the Shumagin segment. (A) The thick black lines show P-T paths at slab mantle depths of C3 anomaly (15 – 25 km sub-*

Moho) using the thermal petrologic model of ref. [3]. *The grey patch indicates the range of possible P-T paths for C3. Dashed thick black lines show P-T conditions at different locations along the slab path. Colored lines show various stability fields from different dehydration experiments for antigorite, chrysotile, and talc (modified from ref.* [55]*). (B) The MT model with the hydrous mineral stability fields overlain. The hydrous mineral in each experiment is stable above the respective curve and unstable (e.g. dehydrated) below the curve. Lines match the legend in (A). References: B86, H03, P05, PN10, UT99, WS97*[34–39]. *Abbreviations: Chr = chrysotile; Atg = antigorite; Br = brucite; Harz = harzburgite; Ta = talc; Fo = forsterite.*

Figure 4*: Conceptual model highlighting primary interpretations of along-dip variation of seismogenic zone behavior into three segments. (1) The relatively fluid-poor segment with seismically-imaged rough patches leading to weak coupling and fault creep. (2) The fluid-rich, conditionally stable segment with fluids derived from forearc slab mantle dehydration. Here, small-scale seismicity is abundant which accommodates interseismic strain via fault creep, but ruptures when triggered by nearby slip. Fluids may escape along the normal fault separating the Prince William and Chugach terranes, but this is unclear from the MT image alone. (3) The relatively fluid-poor, downdip segment with limited seismicity.*

REFERENCES

1. Faccenda, M. Water in the slab: A trilogy. *Tectonophysics* vol. 614 1–30 Preprint at https://doi.org/10.1016/j.tecto.2013.12.020 (2014).
2. Saffer, D. M. & Tobin, H. J. Hydrogeology and mechanics of subduction zone forearcs: Fluid flow and pore pressure. *Annu Rev Earth Planet Sci* **39**, 157–186 (2011).
3. Abers, G. A., van Keken, P. E. & Wilson, C. R. Deep decoupling in subduction zones: Observations and temperature limits. *Geosphere* **16**, 1408–1424 (2020).
4. Heise, W. *et al.* Changes in electrical resistivity track changes in tectonic plate coupling. *Geophys Res Lett* **40**, 5029–5033 (2013).
5. Egbert, G. D. *et al.* Fluid transport and storage in the Cascadia forearc influenced by overriding plate lithology. *Nat Geosci* **15**, 677–682 (2022).
6. Chesley, C., Naif, S., Key, K. & Bassett, D. Fluid-rich subducting topography generates anomalous forearc porosity. *Nature* **595**, 255–260 (2021).
7. Heise, W. *et al.* Electrical resistivity imaging of the inter-plate coupling transition at the Hikurangi subduction margin, New Zealand. *Earth Planet Sci Lett* **524**, (2019).
8. Noda, H. & Lapusta, N. Stable creeping fault segments can become destructive as a result of dynamic weakening. *Nature* **493**, 518–521 (2013).

9. Ichihara, H., Kasaya, T., Baba, K., Goto, T. & Yamano, M. 2D resistivity model around the rupture area of the 2011 Tohoku-oki earthquake (Mw 9.0). *Earth, Planets and Space* **75**, 82 (2023).
10. Park, J. O., Naruse, H. & Bangs, N. L. Along-strike variations in the Nankai shallow décollement properties and their implications for tsunami earthquake generation. *Geophys Res Lett* **41**, 7057–7064 (2014).
11. Wang, K. & Bilek, S. L. Invited review paper: Fault creep caused by subduction of rough seafloor relief. *Tectonophysics* vol. 610 1–24 Preprint at https://doi.org/10.1016/j.tecto.2013.11.024 (2014).
12. Davies, J., Sykes, L., House, L. & Jacob, K. Shumagin seismic gap, Alaska peninsula: history of great earthquakes, tectonic setting, and evidence for high seismic potential. *J Geophys Res* **86**, 3821–3855 (1981).
13. Li, S. & Freymueller, J. T. Spatial Variation of Slip Behavior Beneath the Alaska Peninsula Along Alaska-Aleutian Subduction Zone. *Geophys Res Lett* **45**, 3453–3460 (2018).
14. Jiang, Y., González, P. J. & Bürgmann, R. Subduction earthquakes controlled by incoming plate geometry: The 2020 M > 7.5 Shumagin, Alaska, earthquake doublet. *Earth Planet Sci Lett* **584**, (2022).
15. Shillington, D. J. *et al.* Link between plate fabric, hydration and subduction zone seismicity in Alaska. *Nat Geosci* **8**, 961–964 (2015).
16. Wei, S. S. *et al.* Along-strike variations in intermediate-depth seismicity and arc magmatism along the Alaska Peninsula. *Earth Planet Sci Lett* **563**, (2021).
17. Li, J. *et al.* Downdip variations in seismic reflection character: Implications for fault structure and seismogenic behavior in the Alaska subduction zone. *J Geophys Res Solid Earth* **120**, 7883–7904 (2015).
18. Bécel, A. *et al.* Tsunamigenic structures in a creeping section of the Alaska subduction zone. *Nat Geosci* **10**, 609–613 (2017).
19. Shillington, D. J., Bécel, A. & Nedimović, M. R. Upper Plate Structure and Megathrust Properties in the Shumagin Gap Near the July 2020 M7.8 Simeonof Event. *Geophysical Research Letters* vol. 49 Preprint at https://doi.org/10.1029/2021GL096974 (2022).
20. Acquisto, T., Bécel, A., Singh, S. C. & Carton, H. Evidence of Strong Upper Oceanic Crustal Hydration Outboard the Alaskan and Sumatran Subduction Zones. *J Geophys Res Solid Earth* **127**, (2022).
21. Li, J. *et al.* Connections between subducted sediment, pore-fluid pressure, and earthquake behavior along the Alaska megathrust. *Geology* **46**, 299–302 (2018).

22. Ye, L., Lay, T., Kanamori, H., Yamazaki, Y. & Cheung, K. F. The 22 July 2020 MW 7.8 Shumagin seismic gap earthquake: Partial rupture of a weakly coupled megathrust. *Earth Planet Sci Lett* **562**, (2021).
23. Xiao, Z. *et al.* The deep Shumagin gap filled: Kinematic rupture model and slip budget analysis of the 2020 Mw 7.8 Simeonof earthquake constrained by GNSS, global seismic waveforms, and floating InSAR. *Earth Planet Sci Lett* **576**, (2021).
24. Zhao, B. *et al.* Aseismic slip and recent ruptures of persistent asperities along the Alaska-Aleutian subduction zone. *Nat Commun* **13**, (2022).
25. Liu, C., Lay, T., Xiong, X. & Wen, Y. Rupture of the 2020 MW 7.8 Earthquake in the Shumagin Gap Inferred From Seismic and Geodetic Observations. *Geophys Res Lett* **47**, (2020).
26. Cordell, D. *et al.* Magnetotelluric Data and Resistivity Model for Shumagin Gap, Alaska. Preprint at https://doi.org/10.6084/m9.figshare.21751634 (2022).
27. Naif, S., Key, K., Constable, S. & Evans, R. L. Water-rich bending faults at the Middle America Trench. *Geochemistry, Geophysics, Geosystems* **16**, 2582–2597 (2015).
28. Cordell, D., Unsworth, M. J., Díaz, D. & Reyes-Wagner, V. Fluid and Melt Pathways in the Central Chilean Subduction Zone Near the 2010 Maule Earthquake (35–36°S) as Inferred From Magnetotelluric Data. *Geochemistry, Geophysics, Geosystems* **20**, 1–18 (2019).
29. Guo, X., Yoshino, T. & Katayama, I. Electrical conductivity anisotropy of deformed talc rocks and serpentinites at 3GPa. *Physics of the Earth and Planetary Interiors* **188**, 69–81 (2011).
30. Aretusini, S., Meneghini, F., Spagnuolo, E., Harbord, C. W. & Di Toro, G. Fluid pressurisation and earthquake propagation in the Hikurangi subduction zone. *Nat Commun* **12**, (2021).
31. Hatakeyama, K., Katayama, I., Hirauchi, K. I. & Michibayashi, K. Mantle hydration along outer-rise faults inferred from serpentinite permeability. *Sci Rep* **7**, (2017).
32. Arnulf, A. F. *et al.* Upper-plate controls on subduction zone geometry, hydration and earthquake behaviour. *Nat Geosci* **15**, 143–148 (2022).
33. Cai, C., Wiens, D. A., Shen, W. & Eimer, M. Water input into the Mariana subduction zone estimated from ocean-bottom seismic data. *Nature* **563**, 389–392 (2018).
34. Berman, R. G. ;, Engi, M. ;, Greenwood, H. J. ; & Brown, T. H. Derivation of Internally-Consistent Thermodynamic Data by the Technique of Mathematical Programming: a Review with Application the System MgO-SiO2-H2O. *Journal of Petrology* **27**, (1986).
35. Hacker, B. R., Abers, G. A. & Peacock, S. M. Subduction factory 1. Theoretical mineralogy, densities, seismic wave speeds, and H 2 O contents . *J Geophys Res Solid Earth* **108**, (2003).
36. Perrillat, J. P. *et al.* Kinetics of antigorite dehydration: A real-time X-ray diffraction study. *Earth Planet Sci Lett* **236**, 899–913 (2005).

37. Padrón-Navarta, J. A., Hermann, J., Garrido, C. J., López Sánchez-Vizcaíno, V. & Gómez-Pugnaire, M. T. An experimental investigation of antigorite dehydration in natural silica-enriched serpentinite. *Contributions to Mineralogy and Petrology* **159**, 25–42 (2010).

38. Ulmer, P. & Trommsdorff, V. Phase relations of hydrous mantle subducting to 300 km. in *Mantle Petrology: Field Observations and High Pressure Experimentation: A Tribute to Francis R. (Joe) Boyd* (eds. Fei, Y., Bertka, C. M. & Mysen, B. O.) (The Geochemical Society: Special Publication No. 6, 1999).

39. Wunder, B. & Schreyer, W. Antigorite: High-pressure stability in the system MgO-SiO_2-H_2O (MSH). *Lithos* **41**, 213–227 (1997).

40. Peacock, S. M. Advances in the thermal and petrologic modeling of subduction zones. *Geosphere* **16**, 1647–1663 (2020).

41. Gutiérrez-Aguilar, F., Hernández-Uribe, D., Holder, R. M. & Condit, C. B. Fluid-Induced Fault Reactivation Due To Brucite + Antigorite Dehydration Triggered the Mw7.1 September 19th Puebla-Morelos (Mexico) Intermediate-Depth Earthquake. *Geophys Res Lett* **49**, (2022).

42. Pattison, D. R. M., de Capitani, C. & Gaidies, F. Petrological consequences of variations in metamorphic reaction affinity. *Journal of Metamorphic Geology* **29**, 953–977 (2011).

43. Kohli, A. H. & Warren, J. M. Evidence for a Deep Hydrologic Cycle on Oceanic Transform Faults. *J Geophys Res Solid Earth* **125**, (2020).

44. Wright, N. M., Seton, M., Williams, S. E. & Müller, R. D. The Late Cretaceous to recent tectonic history of the Pacific Ocean basin. *Earth-Science Reviews* vol. 154 138–173 Preprint at https://doi.org/10.1016/j.earscirev.2015.11.015 (2016).

45. Zack, T. & John, T. An evaluation of reactive fluid flow and trace element mobility in subducting slabs. *Chem Geol* **239**, 199–216 (2007).

46. Guo, H. & Keppler, H. Electrical Conductivity of NaCl-Bearing Aqueous Fluids to 900°C and 5 GPa. *J Geophys Res Solid Earth* **124**, 1397–1411 (2019).

47. Korenaga, J. On the extent of mantle hydration caused by plate bending. *Earth Planet Sci Lett* **457**, 1–9 (2017).

48. Park, J. O. *et al.* Seismic Reflection Images of Possible Mantle-Fluid Conduits and Basal Erosion in the 2011 Tohoku Earthquake Rupture Area. *Front Earth Sci (Lausanne)* **9**, (2021).

49. Wiersberg, T., Hammerschmidt, S. B., Fuchida, S., Kopf, A. & Erzinger, J. Mantle-derived fluids in the Nankai Trough Kumano forearc basin. *Prog Earth Planet Sci* **5**, (2018).

50. Abers, Geoffrey. A. Three-dimensional inversion of regional P and S arrival times in the east Aleutians and sources of subduction zone gravity highs. *J Geophys Res* **99**, 4395–4412 (1994).

51. United States Geological Survey. USGS Earthquake Catalog 2010-2021. *Earthquake Hazards Program* https://www.usgs.gov/programs/earthquake-hazards/earthquakes (2022).

52. Horowitz, W. L., Steffy, D. A., Hoose, P. J. & Turner, R. F. *Geologic Report for the Shumagin Planning Area, Western Gulf of Alaska*. (1989).

53. Hayes, G. P. *et al.* Slab2, a comprehensive subduction zone geometry model. *Science (1979)* **362**, 58–61 (2018).

54. Ekström, G., Nettles, M. & Dziewoński, A. M. The global CMT project 2004-2010: Centroid-moment tensors for 13,017 earthquakes. *Physics of the Earth and Planetary Interiors* **200–201**, 1–9 (2012).

55. Ferrand, T. P. Seismicity and mineral destabilizations in the subducting mantle up to 6 GPa, 200 km depth. *Lithos* **334–335**, 205–230 (2019).

METHODS

1 DATA ANALYSIS

Marine MT data were collected along a 250-km profile in the Shumagin segment during a month-long cruise in May-June 2019 aboard the R/V Sikuliaq. The profile was oriented approximately 15°W of north, perpendicular to the Aleutian trench, and collocated with the previous seismic profile Line 5 from the ALEUT project[18]. The profile traversed the incoming plate, the trench, and the forearc shelf, terminating 25 km south of Unga Island. Data were collected at 51 sites along the profile, with 4 km site spacing, using ocean-bottom electromagnetic (OBEM) receivers developed by Scripps Institution for Oceanography[56] with recording times from 11–21 June 2022 (averaging 3–5 days of time-series data) and processed using robust multi-station code[57]. Dimensionality analysis using polar diagrams and phase tensors indicate that the sites in the trench and outer rise (i.e. sites 507 to 538) are very distorted and/or 3-D with phase tensor skews >5° at nearly all sites and frequencies, out-of-quadrant phases at many sites, large diagonal impedance components, and no consistent strike direction (Extended Data Fig. 1, Extended Data Fig. 2, and Extended Data Fig. 3). However, the 23 sites collected on the forearc shelf (i.e. sites 538 to 548) are more well-behaved and amenable to 2-D modelling, with phase tensor skews <5° at many sites and many frequencies, and a more coherent strike direction approximately 75°E of north (i.e. parallel to the trench). As a result, 23 sites on the forearc shelf were used for subsequent 2-D inverse modelling (Extended Data Fig. 2). The 2-D nature of the data suggest that structures beneath the forearc can be approximated to extend laterally along strike (as in 2-D modelling), although a full array of data with 3-D modelling would be required to determine the true lateral extent of such structures. Prior to inversion, data were rotated to geoelectric strike and edited to remove high skew and/or noisy data points. After editing, there is a notable dead band in the data around 10 s. Several sites closer to the trench (i.e. 538a, 538b, and 538c) had some phase tensor skews >5° at long periods, but the off-diagonal data appeared clean and so the sites were not removed in an attempt to increase data coverage. The final edited data set included 410 impedance tensor data at periods from 1 s to 3000 s.

2 MESH DESIGN

TE and TM apparent resistivity and phase data were inverted using the MARE2DEM two-dimensional inversion algorithm[58]. The starting model was constructed with a central rectangular mesh area along the profile from the trench (0 km) to 200 km inboard of the trench, and extending to a depth of 250 km. Model elements were ~750 m x 200 m at the surface with a 1.05 growth factor. Outside the region of interest, a triangular mesh of padding cells extended from -425 km to 650 km relative to the trench axis, and to a depth of 500 km to avoid boundary effects, with cells growing exponentially to avoid excessive computational costs. The Earth was given a uniform value of 100 Ωm, and the air and the ocean were fixed at 10^9 Ωm and 0.3 Ωm, respectively. The rectangular mesh conformed to bathymetry from GMRT Synthesis DEM[59].

3 INVERSIONS

3.1 Preferred Inversion Model

A variety of inversion tests were done to examine the effects of data selection, anisotropy, tears at the slab interface, smoothing, etc. The final, preferred inversion (run40) used an isotropic resistivity which did not include tears, and converged to a root mean square (r.m.s.) target misfit of 1.00 after 30 iterations using 5% error floors on the impedance (see Extended Data Fig. 4). The preferred inversion model is shown in Fig. 2 of the main text. Since the choice of error floor is somewhat arbitrary, the inversion was allowed to continue to run with a target r.m.s. misfit of 0. In this case, it ran for 52 iterations wherein the r.m.s. could not be reduced below 0.962. The modest decrease in r.m.s. came at the expense of much greater model roughness.

The data fit for each of the 23 MT sites is shown in Extended Data Fig. 5 for the 30th iteration (i.e. overall r.m.s. = 1.00), and the misfit breakdown as a function of site, period, and impedance component is shown in Extended Data Fig. 6. The data fits appear to be quite uniform except at three sites: 541a, 543, and 548. These sites contain >15 periods and have poor fits on the TE mode apparent resistivity at all longer periods (>10 s). The effect is subtle visually, but can be seen in Extended Data Fig. 5 where the apparent resistivity is consistently underestimated at Sites 541a and Site 548, and slightly over-estimated at Site 543. The curves themselves are not noisy and look similar to adjacent sites. It is possible that there are some subtle 3-D effects or galvanic distortions at these sites, although standard measures of dimensionality do not indicate strong 3-D effects at these sites relative to adjacent sites.

3.2 Including Slab Tear

Extended Data Fig. 7 shows the results of a model which included a "slab tear" at the plate interface. This tear means that the inversion algorithm is restricted in its ability to apply smoothing across the plate interface boundary. The resulting model has similar overall structure as the preferred inversion with little change to the position of C1, C2, or C3. It is common to apply this type of restriction at the plate interface. However, we chose not to do so for our "preferred inversion" for several reasons.

Firstly, this inversion required 86 iterations in order to converge to an r.m.s. of 1.0 in comparison to the unconstrained inversion which only required 30 iterations. This implies that it is much more difficult for the data to be fit when the constraint is imposed. Secondly, imposing a no-smoothing constraint at the plate boundary implicitly assumes that there ought to be a strong conductivity contrast between the upper plate and the slab. However, this may not always be the case especially if there are conduits which allow fluids to pass through the slab and cross the boundary into the upper plate. The seismic reflection imaging suggests that parts of the plate interface have a relatively weak reflector[18], which makes it hard to define a boundary and suggests that there may not be a strong contrast at the plate interface. Their work also indicates that parts of the plate interface have multiple bands of reflectors which they interpreted as fluids above/within/through the plate. These facts suggest that imposing a strong gradient at the plate interface may lead to erroneous results and we prefer our inversion to have fewer *a priori* constraints.

3.3 The Lithosphere-Asthenosphere Boundary Anomaly

Although not discussed in the main text since it is beyond the scope of this paper, we note that there is a deeper anomaly which appears in the inversions on the trenchward side of the profile (i.e. <100 km from the trench) at a depth of about 100 km, consistent with the depth to the lithosphere-asthenosphere boundary (LAB) and similar to features observed elsewhere[60]. Extended Data Fig. 8 shows the full model space for the preferred inversion. While the shelf MT data are sensitive to the presence of an LAB conductor (see section 3.3.3 below), the anomaly is located at the edge of our data coverage and extends beneath the incoming plate, beyond the subset of MT sites that we inverted.

3.4 Sensitivity Tests

We also examined how the data respond when the different interpreted features are “removed”. Here we examine three features: the plate interface conductor (C2), the slab mantle conductor (C3), and the deeper LAB conductor (C4).

3.4.1 Plate Interface Conductor

The plate interface conductor was replaced with 100 Ωm, the starting halfspace value (Extended Data Fig. 9a). After this feature was removed, the forward response of this edited model had an r.m.s. misfit of 1.28 (compared to original misfit of 1.0). There was a significant increase in r.m.s. misfit on sites 540c through 547, particularly on the TE mode apparent resistivity (Extended Data Fig. 10). For example, the r.m.s. misfit on site 543 increased from 1.19 to 2.42. This primarily impacted periods from about 25 s to 500 s. This large change in r.m.s. misfit at multiple sites and at multiple periods confirm that the data are highly sensitive to this feature.

3.4.2 Slab Mantle Conductor

The slab mantle conductor was replaced with 100 Ωm, the starting halfspace value (Extended Data Fig. 9b). After this feature was removed, the forward response of this edited model had an r.m.s. misfit of 1.37 (compared to original misfit of 1.0). This was the largest increase in r.m.s. misfit of all the sensitivity tests, suggesting that this conductor has the greatest overall impact on the data. There was a significant increase in r.m.s. misfit on nearly all sites inboard of site 539a, particularly on the TE mode apparent resistivity and TE mode phase (Extended Data Fig. 10). This primarily impacted periods from about 100 s to 1000 s. Interestingly, the r.m.s. misfit decreased somewhat at sites 541a and 548 (two of the sites which had anomalously large r.m.s. misfit on the TE mode apparent resistivity in the original inversion), while significantly increasing the r.m.s. on site 543. This further suggests some unique 3-D effects wherein the data struggle to adequately fit this feature with a 2-D assumption using a global r.m.s. misfit (despite the data themselves appearing relatively 2-D by all metrics).

3.4.3 LAB Conductor

The deeper conductor at the LAB was not interpreted in this study, but a sensitivity test was performed to examine how much it impacts the data relative to the other interpreted features (C2 and C3). The LAB conductor was replaced with 100 Ωm, the starting halfspace value (Extended Data Fig. 9c). After this feature was removed, the forward response of this edited model had an r.m.s. misfit of 1.15 (compared to original misfit of 1.0). This was the smallest change in overall misfit of the three tests, suggesting that the LAB conductor has a smaller influence on the data than C2 and C3.. The r.m.s. misfit increased slightly at nearly all sites, but only affected the longest periods >1000 s, particularly on the TE mode apparent resistivity and phase (Extended Data Fig. 10).

DATA AVAILABILITY

MT impedance data and inversion model files are available at https://doi.org/10.6084/m9.figshare.21751634

METHODS-ONLY REFERENCES

56. Constable, S. Review paper: Instrumentation for marine magnetotelluric and controlled source electromagnetic sounding. *Geophys Prospect* **61**, 505–532 (2013).
57. Egbert, G. D. Robust multiple-station magnetotelluric data processing. *Geophys J Int* **130**, 475–496 (1997).
58. Key, K. MARE2DEM: a 2-D inversion code for controlled source electromagnetic and magnetotelluric data. *Geophys J Int* **207**, 571–588 (2016).
59. Ryan, W. B. F. *et al.* Global Multi-Resolution Topography (GMRT) synthesis data set. *Geochemistry, Geophysics, Geosystems* **10**, Q03014 (2009).
60. Naif, S., Key, K., Constable, S. & Evans, R. L. Melt-rich channel observed at the lithosphere–asthenosphere boundary. *Nature* **495**, 356–359 (2013).

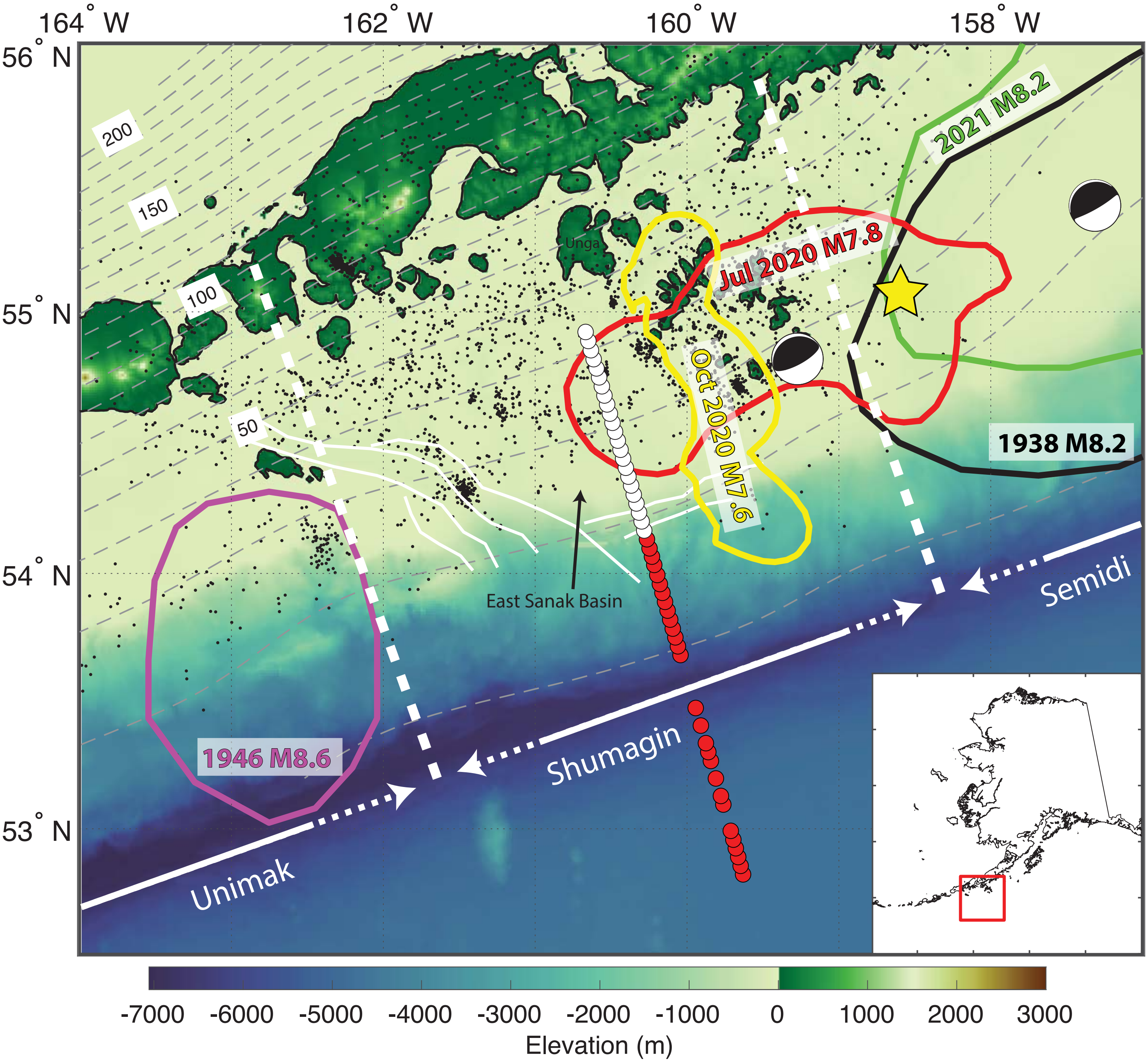

164° W
162° W
160° W
158° W
56° N
55° N
54° N
53° N
200
150
100
50
Unga
East Sanak Basin
Jul 2020 M7.8
Oct 2020 M7.6
2021 M8.2
1938 M8.2
1946 M8.6
Semidi
Shumagin
Unimak
-7000
-6000
-5000
-4000
-3000
-2000
-1000
0
1000
2000
3000
Elevation (m)

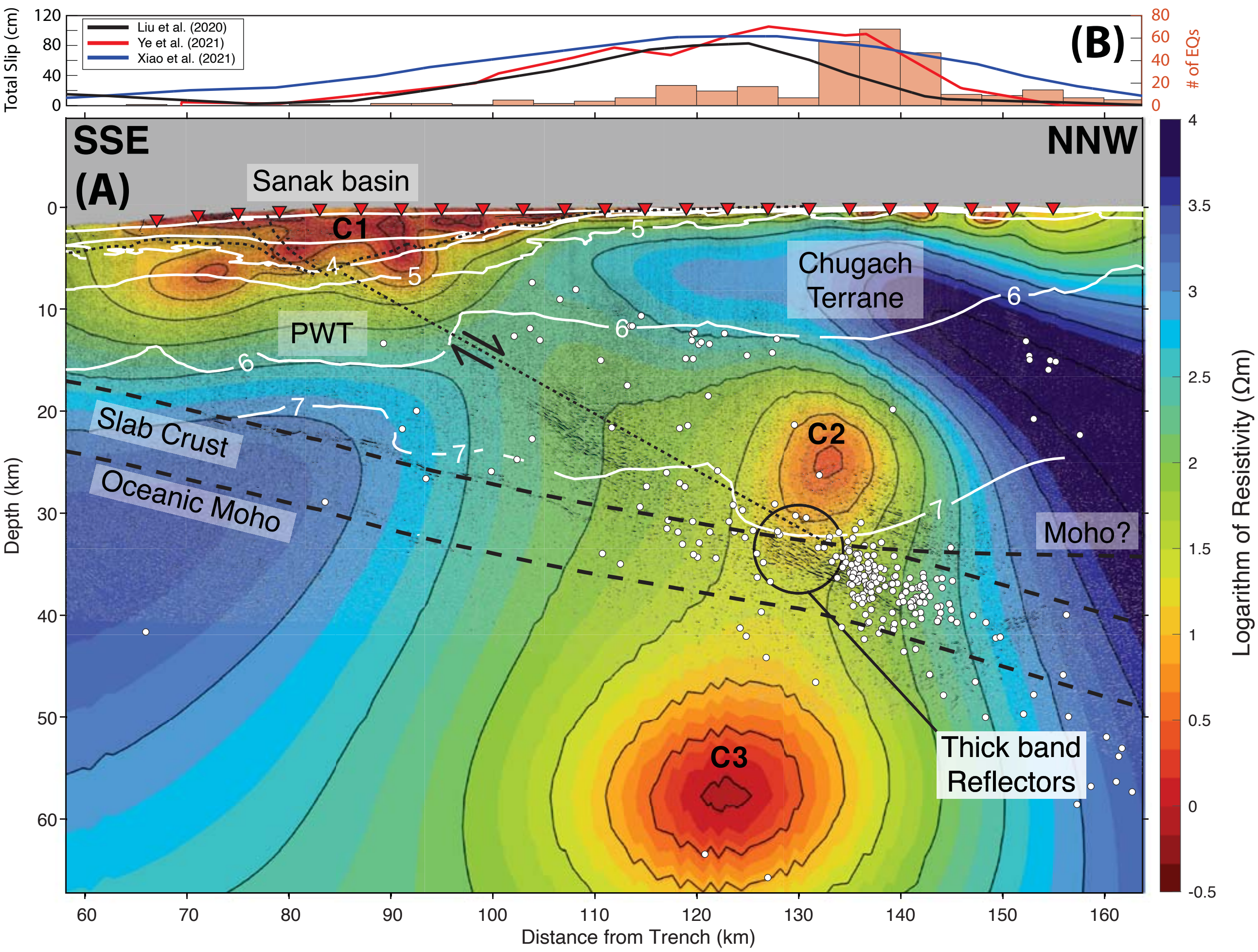

Total Slip (cm)
# of EQs
Liu et al. (2020)
Ye et al. (2021)
Xiao et al. (2021)
(B)
SSE
(A)
NNW
Sanak basin
C1
Chugach
Terrane
PWT
C2
Slab Crust
Oceanic Moho
Moho?
C3
Thick band
Reflectors
Depth (km)
Distance from Trench (km)
Logarithm of Resistivity (Ωm)

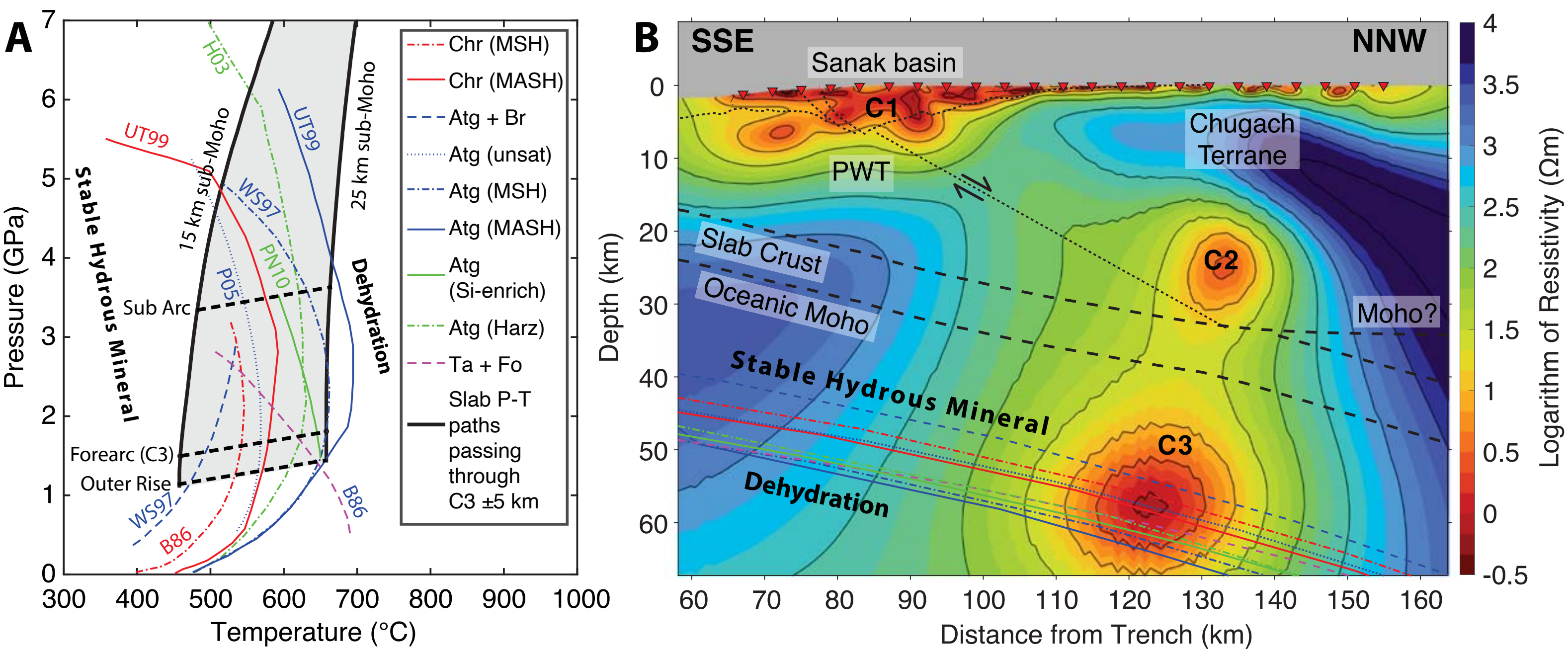
A
B
Pressure (GPa)
Temperature (°C)
Stable Hydrous Mineral
Dehydration
15 km sub-Moho
25 km sub-Moho
Sub Arc
Forearc (C3)
Outer Rise
UT99
WS97
P05
PN10
Hi03
B86
Chr (MSH)
Chr (MASH)
Atg + Br
Atg (unsat)
Atg (MSH)
Atg (MASH)
Atg (Si-enrich)
Atg (Harz)
Ta + Fo
Slab P-T paths passing through C3 ±5 km
SSE
NNW
Sanak basin
C1
C2
C3
PWT
Chugach Terrane
Slab Crust
Oceanic Moho
Moho?
Depth (km)
Distance from Trench (km)
Logarithm of Resistivity (Ωm)

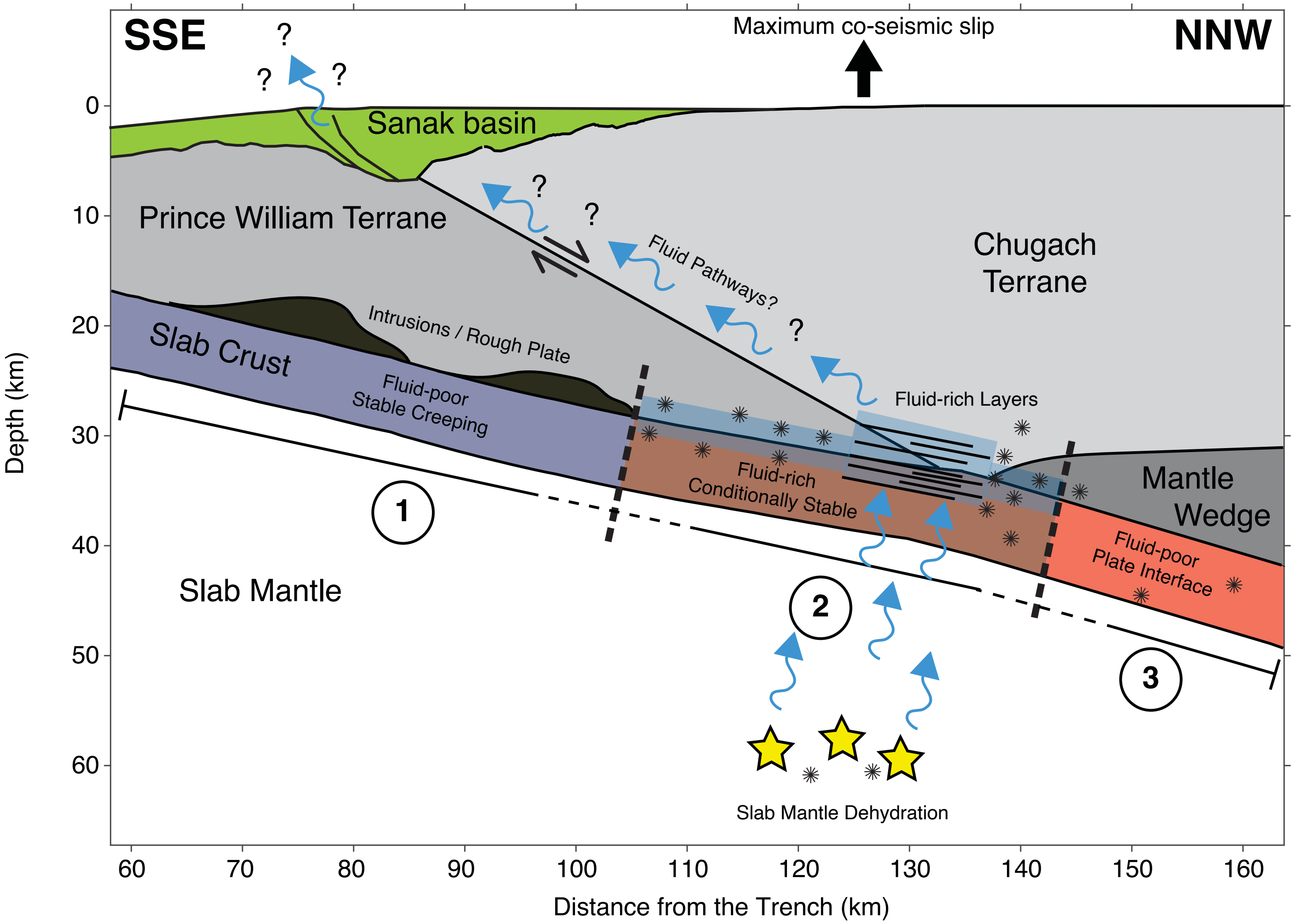

SSE
NNW
Maximum co-seismic slip
?
?
?
Sanak basin
Prince William Terrane
?
?
Fluid Pathways?
?
Chugach
Terrane
Intrusions / Rough Plate
Slab Crust
Fluid-poor
Stable Creeping
Fluid-rich Layers
Fluid-rich
Conditionally Stable
Mantle
Wedge
Fluid-poor
Plate Interface
1
2
3
Slab Mantle
Slab Mantle Dehydration
Depth (km)
0
10
20
30
40
50
60
60
70
80
90
100
110
120
130
140
150
160
Distance from the Trench (km)

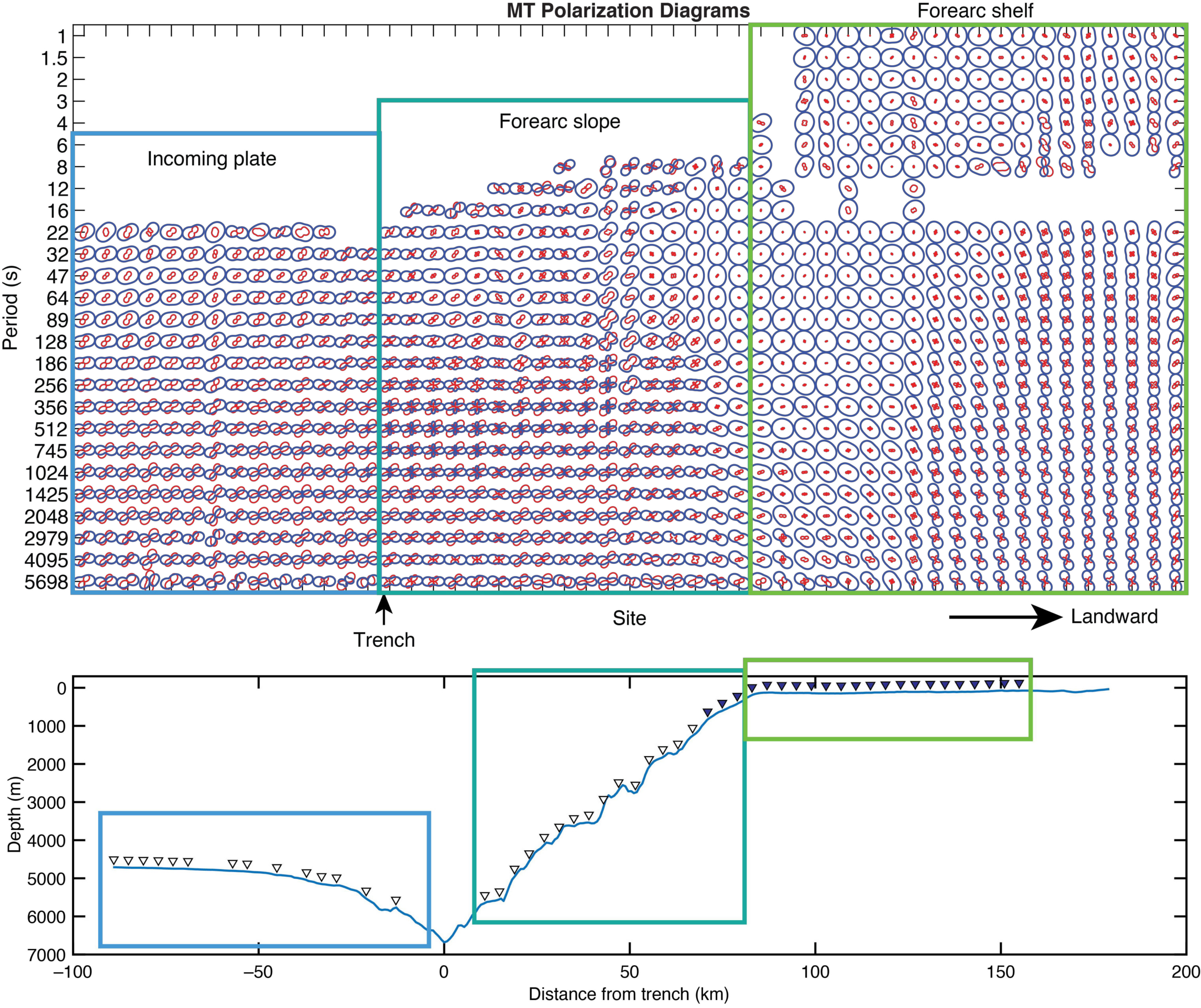
MT Polarization Diagrams
Forearc shelf
Forearc slope
Incoming plate
Period (s)
1
1.5
2
3
4
6
8
12
16
22
32
47
64
89
128
186
256
356
512
745
1024
1425
2048
2979
4095
5698
Trench
Site
Landward
Depth (m)
0
1000
2000
3000
4000
5000
6000
7000
−100
−50
0
50
100
150
200
Distance from trench (km)